

Healthy versus Pathological Learning Transferability in Shoulder Muscle MRI Segmentation using Deep Convolutional Encoder-Decoders

Pierre-Henri Conze*, Sylvain Brochard, Valérie Burdin, Frances T. Sheehan and Christelle Pons

Abstract—Automatic segmentation of pathological shoulder muscles in patients with musculo-skeletal diseases is a challenging task due to the huge variability in muscle shape, size, location, texture and injury. A reliable fully-automated segmentation method from magnetic resonance images could greatly help clinicians to plan therapeutic interventions and predict interventional outcomes while eliminating time consuming manual segmentation efforts. The purpose of this work is three-fold. First, we investigate the feasibility of pathological shoulder muscle segmentation using deep learning techniques, given a very limited amount of available annotated pediatric data. Second, we address the learning transferability from healthy to pathological data by comparing different learning schemes in terms of model generalizability. Third, extended versions of deep convolutional encoder-decoder architectures using encoders pre-trained on non-medical data are proposed to improve the segmentation accuracy. Methodological aspects are evaluated in a leave-one-out fashion on a dataset of 24 shoulder examinations from patients with obstetrical brachial plexus palsy and focus on 4 different muscles including deltoid as well as infraspinatus, supraspinatus and subscapularis from the rotator cuff. The most relevant segmentation model is partially pre-trained on ImageNet and jointly exploits inter-patient healthy and pathological annotated data. Its performance reaches Dice scores of 82.4%, 82.0%, 71.0% and 82.8% for deltoid, infraspinatus, supraspinatus and subscapularis muscles. Absolute surface estimation errors are all below 83mm² except for supraspinatus with 134.6mm². These contributions offer new perspectives for force inference in the context of musculo-skeletal disorder management.

Index Terms—Shoulder muscle segmentation, musculo-skeletal disorders, deep convolutional encoder-decoders, healthy versus pathological transferability, obstetrical brachial plexus palsy

I. INTRODUCTION

Pixel-wise segmentation is a crucial task in medical image analysis with many applications such as computer-assisted diagnosis, surgery planning, visual augmentation, image-guided interventions or extraction of quantitative indices from images. The rapid development of non-invasive imaging technologies over the last decades has opened new horizons in studying both healthy and pathological anatomy. However, the analysis of complex Magnetic Resonance (MR)

imaging datasets could be tedious and time-consuming for radiologist, clinicians or researchers. Thus, computerized assistance methods including robust automatic image segmentation techniques are needed to guide and improve image interpretation and clinical decision making.

In particular, the need for accurate muscle delineations emerges for the management of musculo-skeletal disorders. The task becomes difficult when the pathology alters the size, shape, texture and global MR appearance of muscles, especially when a large variability across patients arises due to age-related development and injury. Obstetrical brachial plexus palsy (OBPP), one of the most common birth injury [1], is such a pathology. As for many other musculo-skeletal diseases affecting children or adults, the limited amount of available data in OBPP represents an additional challenge.

Characterized by the disorder of the peripheral nervous system conducting signals from the spinal cord to shoulders, arms and hands, OBPP occurs most often during the delivery phase when lateral tractions are applied to the head to permit shoulder clearance [2]. Its incidence is estimated around 1.4 every 1000 live births [3]. While full recovery is possible, prognosis is variable and up to 35% of children may have from weak to severe life-long functional impairments [2]. Shoulder involvement is the main cause of morbidity. At this level, nerve injuries lead to variable muscle denervations and induce muscle degeneration with fatty and fibrosis infiltration, disruption of growth, muscle atrophy and force imbalances between agonist and antagonist muscle pairs [4].

Treatment and prevention of shoulder muscle strength imbalances are main therapeutic goals for children with OBPP who do not fully recover [5]. Therapeutic interventions mainly aim at restoring a physiological balance between muscles length and strength to prevent or treat joint deformity and facilitate movement of the upper limb [6]. Patient-specific information related to the degree of muscle atrophy across shoulder muscles is therefore needed to plan interventions and predict interventional outcomes [7]. However, clinical examinations do not allow the distinction and precise evaluation of each shoulder muscle. Conversely, recent works report a clear relationship between muscle atrophy and strength loss for children with OBPP [1], showing the need for muscle morphological evaluation to better understand and treat shoulder problems. In this direction, shoulder muscle segmentation on MR images is useful to both quantify individual muscle involvement and analyze shoulder strength balance profiles of non-dominant and dominant shoulders for children with OBPP.

P.-H. Conze is with IMT Atlantique, Inserm UMR 1101, Brest, France. E-mail: pierre-henri.conze@imt-atlantique.fr. S. Brochard is with Rehabilitation Medicine Department, University Hospital of Brest, Inserm UMR 1101, Fondation ILDYS, Brest, France. E-mail : sylvain.brochard@chu-brest.fr. V. Burdin is with IMT Atlantique, Inserm UMR 1101, Brest, France. E-mail: valerie.burdin@imt-atlantique.fr. F. T. Sheehan is with Rehabilitation Medicine, National Institutes of Health, Bethesda, USA. E-mail : gavel-lif@cc.nih.gov. C. Pons is with SSR pediatric, Fondation ILDYS, Brest, France. E-mail : christelle.ponsbecmeur@ildys.org. *Asterisk indicates corresponding author.* Manuscript received — XX, 2017; revised — XX, 2017.

Considering the large variability in shoulder muscle shape, size, location, texture and injury, muscle segmentation from MR images has been commonly noticed as challenging [8]. Both healthy and pathological muscles are prone to subtle or more severe changes regarding their visual properties and could be difficult to delineate near their insertion areas due to the vicinity with other structures (Fig.1). In the case of pathological muscles, changes in muscle shape and signal occur because of muscle degeneration which can render identification of muscle boundaries even more difficult. To circumvent these difficulties, muscle segmentation is traditionally performed manually in a slice-by-slice fashion [9]. However, manual segmentation is a time-consuming task, prone to errors due to intra and inter-expert variability. There has been a recent and growing interest in developing fully-automated techniques for muscle segmentation. This question is all the more significant as many efforts have been recently devoted to pixel-wise segmentation based on deep learning techniques using convolutional encoder-decoders [10].

In this direction, the purpose of our study is three-fold. First, we aim at studying the feasibility of automatic pathological shoulder muscle segmentation using deep convolutional encoder-decoder networks, given the small amount of available annotated data in children with OBPP. To our knowledge, shoulder muscle delineations have never been achieved automatically through deep learning techniques. Second, our work addresses the learning transferability from healthy to pathologic data and focuses in particular on how data available on both healthy and pathological shoulder muscles can be jointly exploited for pathological shoulder muscle delineation. Third, extended versions of deep convolutional encoder-decoder architectures using encoders pre-trained on non-medical data are investigated to improve the segmentation accuracy. Experiments extend preliminary results [11] to four shoulder muscles including deltoid, infraspinatus, supraspinatus and subscapularis. Our contributions reach a robust and fully-automated muscle segmentation pipeline which provides new insights for the management of musculo-skeletal diseases.

II. RELATED WORKS

To get quantitative muscle volume measures, from which forces can be derived [1], muscle segmentation is traditionally performed manually in a slice-by-slice fashion [9] from MR images. This task is extremely time-consuming and requires tens of minutes to get accurate delineations for one single muscle. It is not usable for a great amount of data in research and clinical practice. In addition, manual segmentation is prone to intra and inter-expert variability given the variability of muscle shapes and the lack of clearly visible boundaries between muscles and surrounding anatomy [12]. To ease the process, a semi-automatic processing based on transversal propagations of manually-drawn masks can be considered [13]. It consists of several ascending and descending non-linear registrations applied to manual masks to finally achieve volumetric results in less time than entire manual segmentation.

A model-based muscle segmentation incorporating a prior statistical shape model can be employed to delineate muscles

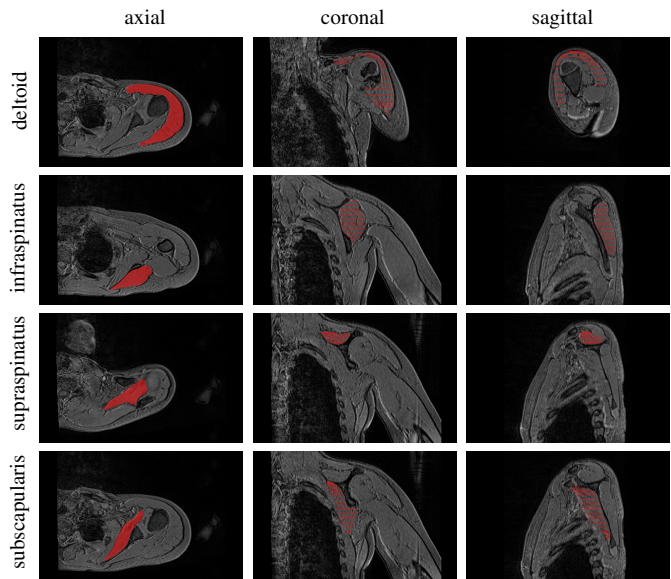


Fig. 1: Groundtruth segmentations of pathological shoulder muscles including deltoid as well as infraspinatus, supraspinatus and subscapularis from the rotator cuff. Axial, coronal and sagittal slices are extracted from a 3D MR examination acquired for a child with obstetrical brachial plexus palsy.

boundaries in MR images. A patient-specific 3D geometry is thus reached based on the deformation of a parametric ellipse fitted to muscle contours, starting from a reduced set of initial slices [14], [15]. Segmentation models can be further improved by exploiting a-priori knowledge of shape information relying on internal shape fitting and auto-correction to guide muscle delineation [16]. Baudin et al. associated in [17] a statistical shape atlas with a random walks graph-based algorithm to automatically segment individual muscles through iterative linear optimization. Andrews et al. [18] used a probabilistic shape representation called generalized log-ratio representation that included adjacency information along with a rotationally invariant boundary detector to segment thigh muscles.

Aligning and merging manually segmented images into specific atlas coordinate spaces can be a reliable alternative. In this context, various single and multi-atlas methods have been proposed for quadriceps muscle segmentation [19], [20] relying on non-linear registration. Engstrom et al. [21] used a statistical shape model constrained using probabilistic MR atlases to automatically segment quadratus lumborum. Segmentation of muscle versus fatty tissues has been also performed through possibilistic clustering [22], histogram-based thresholding followed by region growing [23] and active contours [24] techniques. However, all the previously described methods (except [18]) are not perfectly suited for high inter-subject shape variability and significant differences of tissue appearance due to injury. Moreover, many of the previously described methods are semi-automatic and hence require prior knowledge, usually associated with high computational costs.

Therefore, developing an accurate and robust muscle segmentation method remains an open and challenging issue, especially when dealing with pathological pediatric data. Huge progress has been recently made for automatic image seg-

mentation using deep Convolutional Neural Networks (CNN). Introduced in [25], deep CNNs are entirely data-driven supervised learning models formed by multi-layer neural networks. In contrast to conventional machine learning which requires hand-crafted features and hence specialized knowledge, deep CNNs automatically learn complex hierarchical features directly from data. CNNs obtained outstanding performance for many medical image segmentation tasks [10] which suggests that robust fully-automated delineation of shoulder muscles from MR images may be achieved using CNN-based segmentation. To our knowledge, no other study has been conducted on shoulder muscle segmentation using deep learning methods.

III. METHOD

A. Deep convolutional encoder-decoders

The simplest way to perform segmentation using deep CNNs consists in classifying each pixel individually by working on patches extracted around them [26]. Since input patches from neighboring pixels have large overlaps, the same convolutions are computed many times. By replacing fully connected layers with convolutional layers, a Fully Convolutional Network (FCN) can take entire images as inputs and produce likelihood maps instead of single pixel outputs. It removes the need to select representative patches and eliminates redundant calculations due to patch overlaps. To avoid outputs with far lower resolution than input shapes, FCNs can be applied to shifted versions of input images [27]. Multiple resulting outputs are stitched together to get results at full resolution.

Further improvements can be reached with architectures comprising a regular FCN to extract features and capture context, followed by an up-sampling part that enables to recover the input resolution using up-convolutions [10]. Compared to patch-based or *shift-and-stitch* methods, it allows a precise localization in one single pass while taking into account the full image context. Such architecture consisting of paired networks is called Convolutional Encoder-Decoder (CED).

U-Net [28] is the most well-known CED in the medical image analysis community. U-Net has a symmetrical architecture with equal amount of down-sampling and up-sampling layers between contracting and expanding paths (Fig.3a). The encoder gradually reduces the spatial dimension with pooling layers whereas the decoder gradually recovers object details and spatial dimension. One key aspect of U-Net is the use of *skip connections* which concatenate features from the encoder to the decoder to help in recovering object details better while improving localization accuracy. By allowing information to flow directly from low-level to high-level feature maps, faster convergence is achieved. This architecture can be exploited for 3D volume segmentation [29] by replacing all 2D operations with their 3D counterparts but at the cost of computational speed and GPU memory consumption. Processing 2D slices independently before reconstructing 3D medical volumes remains a simpler alternative. Instead of cross-entropy measures used as loss function, the extension of U-Net proposed in [30] directly minimizes a segmentation error measure to to handle class imbalance between foreground and background.

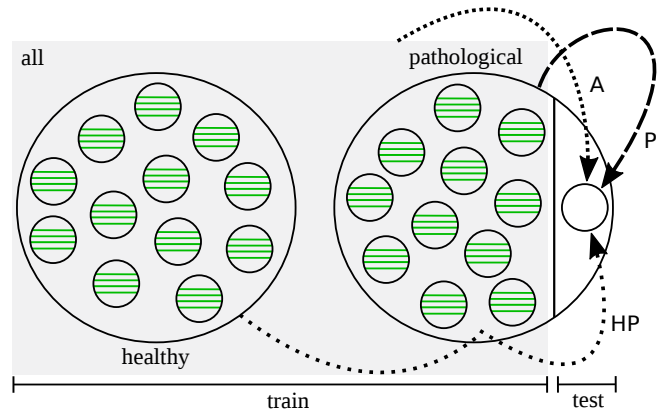


Fig. 2: Three different learning schemes (P, HP, A) involved in a leave-one-out setting for deep learning-based pathological shoulder muscle segmentation.

B. Healthy versus pathological learning transferability

In this work, we investigate the feasibility of automatic pathological shoulder muscle segmentation using deep CEDs (Sect.III-A), given a small amount of available annotated data. In the OBPP context, the availability of both healthy and pathological data for image segmentation brings new queries related to the learning transferability from healthy to pathological structures. This aspect is particularly suitable to musculo-skeletal pathologies for two reasons. First, despite different shapes and sizes due to growth and atrophy, healthy and pathological muscles may share common characteristics such as anatomic locations and overall aspects. Second, such medical applications suffer from a limited amount of available annotated data, usable for segmentation purposes. Combining healthy and pathological data for deep learning-based segmentation can thus act as a smart data augmentation strategy.

In exploring the joint use of healthy and pathological data for pathological muscle segmentation, determining the optimal learning scheme is crucial. Thus, three different learning schemes (Fig.2) employed with deep CEDs are considered:

- **pathological only (P)**: the most common configuration consists in exploiting groundtruth annotations made on impaired shoulder muscles only, assuming that CED features extracted from healthy examinations are not suited enough for pathological anatomies.
- **healthy transfer to pathological (HP)**: another strategy deals with transfer learning and fine tuning from healthy to pathological muscles. In this context, a first CED is trained using groundtruth segmentations from unaffected shoulders only. The weights of the resulting model are then used as initialization for a second CED network which is trained using pathological inputs only.
- **simultaneous healthy and pathological (A)**: the last configuration consists in training a CED with a groundtruth dataset comprising annotations made on both healthy and pathological shoulder muscles, which allows to benefit from a more consequent dataset.

By comparing these different training strategies, we evaluate the benefits brought by combining healthy and pathological data together in terms of model generalizability. The balance between data augmentation and healthy versus pathological

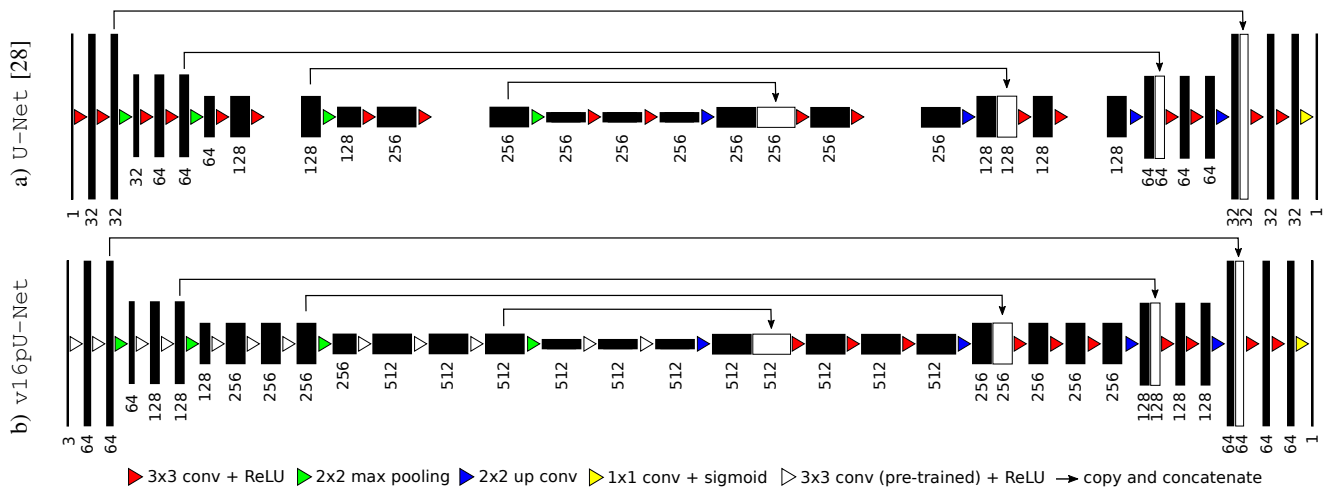


Fig. 3: Extension of U-Net [28] by exploiting as encoder a slightly modified VGG-16 [31] with weights pre-trained on ImageNet [32], following [33], [34]. The decoder is modified to get an exactly symmetrical construction while keeping *skip connections*.

muscle variability is a crucial question which has never been investigated for muscle segmentation. These three different schemes, referred as P (pathological only), HP (healthy transfer to pathological) and A (simultaneous healthy and pathological), are illustrated Fig.2 in a leave-one-out setting. The overall shoulder dataset is divided into healthy and pathological MR examinations. Iteratively, one pathological examination is extracted from the pathological dataset and considered as test examination for muscle segmentation. It will therefore not be used for training contrary to remaining pathological images.

C. Extended architectures with pre-trained encoders

Contrary to deep classification networks which are usually pre-trained on a very large image dataset, CED architectures used for segmentation are typically trained from scratch, relying on randomly initialized weights. Reaching a generic model without over-fitting is therefore tedious, especially when only a small amount of images is available. As suggested in [33], the encoder part of a deep CED network can be replaced by a well-known classification network whose weights are pre-trained on an initial classification task. It allows to exploit transfer learning from large datasets such as ImageNet [32] for deep learning-based segmentation. In the literature, the encoder part of a deep CED has been already replaced by pre-trained VGG-11 [33] and ABN WideResnet-38 [34] with improvements compared to their randomly weighted counterparts.

Following this idea, we propose to extend the standard U-Net architecture (Sect.III-A) by exploiting another simple network from the VGG family [31] as encoder, namely the VGG-16 architecture. To improve performance, this encoder branch is pre-trained on ImageNet [32]. This database has been designed for object recognition purposes and contains more than 1 million natural images from 1000 classes. Pre-training our deep CED dedicated to muscle image segmentation using non-medical data is an efficient way to reduce the data scarcity issue while improving model generalizability [35]. Pre-trained models can not only improve predictive performance but also require less training time to reach convergence for the target task. In particular, low-level features captured by first convolu-

tional layers are usually shared between different image types which explains the success of transfer learning between tasks.

The VGG-16 encoder (Fig.3b) consists of sequential layers including 3×3 convolutional layers followed by Rectified Linear Unit (ReLU) activation functions. Reducing the spatial size of the representation is handled by 2×2 max pooling layers. Compared to standard U-Net (Fig.3a), the first convolutional layer generates 64 channels instead of 32. As the network deepens, the number of channels doubles after each max pooling until it reaches 512 (256 for classical U-Net). After the second max pooling operation, the number of convolutional layers differ from U-Net with patterns of 3 consecutive convolutional layers instead of 2, following the original VGG-16 architecture. In addition, input images are extended from one single greyscale channel to 3 channels by repeating the same content in order to respect the dimensions of the RGB ImageNet images used for encoder pre-training. The only differences with VGG-16 rely in the fact that the last convolutional layer as well as top layers including fully-connected layers and softmax have been omitted. The two last convolutional layers taken from VGG-16 serve as central part of the CED and separate both contracting and expanding paths.

The extension of the U-Net encoder is transferred to the decoder branch by adding 2 convolutional layers as well as more features channels to get an exactly symmetrical construction while keeping *skip connections*. Contrary to encoder weights which are initialized using pre-training performed on ImageNet, decoder weights are set randomly before fine tuning. As for U-Net, a final 1×1 convolutional layer followed by a sigmoid activation function achieves pixel-wise segmentation masks whose resolution are the same as input slices.

IV. DATA AND EXPERIMENTAL RESULTS

A. Imaging dataset

Experimental data have been collected from a previous study [1] investigating the muscle volume-strength relationship in 12 children with unilateral OPBB (averaged age 12.1 ± 3.3 years). In this IRB approved study, informed consents and

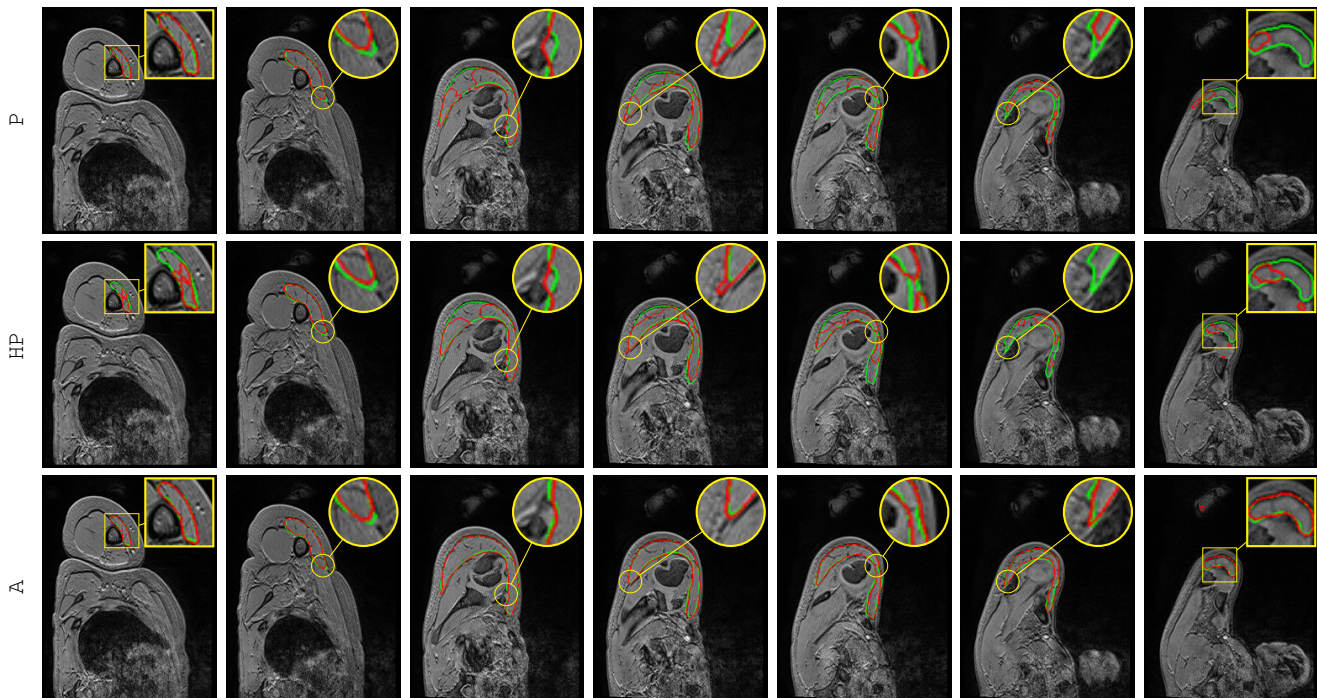


Fig. 4: Pathological deltoid segmentation using U-Net [28] embedded with learning schemes P, HP and A. Groundtruth and estimated delineations are in green and red. Displayed results cover the whole muscle spatial extent for L-P-0103 examination.

assents have been obtained for all subjects. For each patient, two 3D axial-plane T1-weighted gradient-echo MR images have been acquired: one for the affected shoulder and another for the unaffected one. For each healthy or pathological MR image, spatially equally distributed 2D axial slices have been selected for four different shoulder muscles including deltoid as well as infraspinatus, supraspinatus and subscapularis from the rotator cuff. These slices were annotated by an expert in pediatric physical medicine and rehabilitation to reach pixel-wise groundtruth delineations. Image size for axial slices are constant for each subject (416×312 pixels). Image resolution varies from 0.55×0.55 to 0.63×0.63 mm, allowing a finer resolution for smaller subjects. The number of axial slices fluctuates from 192 to 224 whereas slice thickness remains unchanged (1.2mm). Overall, we have 374 (resp. 395) annotated axial slices for deltoid, 306 (367) for infraspinatus, 238 (208) for supraspinatus and 388 (401) for subscapularis across 2400 (2448) axial slices arising from 12 pathological (healthy) examinations. Among these 24 MR images, pairings between affected and unaffected shoulders are known. Due to sparse annotations (Fig.1), deep CEDs exploit as inputs 2D axial slices and produce 2D segmentation masks which can be then stacked to recover a 3D volume for clinical purposes. Among pathological examinations, 8 are right shoulders (R-P-0134, 0684, 0382, 0447, 0660, 0737, 0667, 0277) whereas 4 correspond to left shoulders (L-P-0103, 0351, 0922, 0773). Training images displaying a right (left) shoulder are flipped when a left (right) shoulder is considered for test.

B. Segmentation assessment

To assess both healthy versus pathological learning transferability (Sect.IV-C) and extended pre-trained deep convo-

lutional architectures (Sect.IV-D), the accuracy of automatic pathological shoulder muscle segmentation is quantified based on Dice ($\frac{2TP}{2TP+FP+FN}$), sensitivity ($\frac{TP}{TP+FN}$), specificity ($\frac{TN}{TN+FP}$) and Jaccard ($\frac{TP}{TP+FP+FN}$) similarity scores where TP, FP, TN and FN are the number of true or false positive and negative pixels. We also exploit an absolute surface estimation error (ASE) which compares groundtruth and estimated muscle surfaces defined in mm^2 from segmentation masks. These scores tend to provide a complete assessment of the ability of CED models to provide contours identical to those manually performed. Results provided are averaged among all annotated slices arising from the 12 pathological shoulder examinations.

C. Healthy versus pathological learning transferability

The learning transferability from healthy to pathological data (Sect.III-B) is addressed by comparing learning schemes P (pathological only), HP (healthy transfer to pathological) and A (simultaneous healthy and pathological) in a leave-one-out fashion (Fig.2). To avoid any bias for HP/A, annotated data from the healthy shoulder of the patient whose pathological shoulder is considered for test is not used during training.

For all schemes, deep CED networks are trained using data augmentation since the amount of available training data is limited. To teach the network the desired invariance and robustness properties [28], training 2D axial slices undergo random scaling, rotation, shearing and shifting on both directions. 100 augmented images are thus produced for one single training axial slice. Comparisons between P, HP and A schemes are performed using standard U-Net [28] with 10 epochs, a batch size of 10 images, an *Adam* optimizer with 10^{-4} as learning rate for stochastic optimization, a fuzzy Dice score as loss function and randomly initialized weights for

metric	scheme network	P	HP	A		
				U-Net [28]	v16U-Net	v16pU-Net
dice	deltoid	68.94±29.9	71.05±29.5	<u>78.32±24.4</u>	80.05±23.1	82.42±20.4
	infraspinatus	71.38±24.7	77.00±22.5	<u>81.58±18.3</u>	81.91±19.0	81.98±18.6
	supraspinatus	64.94±28.0	<u>65.69±29.6</u>	65.68±30.7	67.30±29.4	70.98±28.7
	subscapularis	78.10±18.1	74.55±25.2	<u>81.41±15.0</u>	81.58±15.2	82.80±14.4
sens	deltoid	70.85±30.5	70.74±29.5	<u>78.92±25.4</u>	81.45±23.7	83.80±21.3
	infraspinatus	72.12±26.4	79.45±23.1	84.61±18.2	83.74±18.6	83.48±19.0
	supraspinatus	64.02±31.8	63.16±33.2	<u>65.55±34.5</u>	67.21±33.0	68.60±32.3
	subscapularis	78.89±19.7	74.75±27.3	<u>82.53±18.1</u>	81.75±18.8	84.36±16.5
spec	deltoid	99.61±0.80	99.56±1.07	<u>99.85±0.19</u>	99.82±0.22	99.84±0.22
	infraspinatus	99.82±0.23	99.82±0.22	<u>99.84±0.18</u>	99.86±0.17	99.86±0.18
	supraspinatus	99.86±0.18	<u>99.90±0.13</u>	99.88±0.15	99.86±0.17	99.91±0.12
	subscapularis	99.86±0.13	99.83±0.28	<u>99.87±0.13</u>	99.88±0.12	99.86±0.15
jacc	deltoid	59.27±29.7	61.68±29.3	<u>69.48±26.0</u>	71.46±24.9	74.00±22.8
	infraspinatus	60.32±25.6	66.91±24.0	<u>72.00±20.4</u>	72.63±20.6	72.71±21.0
	supraspinatus	53.61±27.1	55.27±29.3	<u>55.70±30.1</u>	56.98±28.7	61.31±28.7
	subscapularis	66.93±19.6	64.31±24.7	<u>70.83±17.6</u>	71.13±17.7	72.72±17.16
ASE	deltoid	252.0±421.6	268.0±507.8	<u>105.5±178.9</u>	94.23±139.2	80.38±127.5
	infraspinatus	156.8±228.7	92.37±105.9	74.47±92.8	80.11±96.2	79.17±96.9
	supraspinatus	174.8±164.0	159.9±153.5	<u>153.9±146.0</u>	147.5±129.4	134.6±135.5
	subscapularis	<u>94.56±95.5</u>	102.0±110.7	95.19±109.0	94.06±111.3	82.95±86.88

TABLE I: Quantitative assessment of deep CEDs (U-Net [28], v16U-Net, v16pU-Net) embedded with learning schemes P, HP and A over the pathological dataset in Dice, sensitivity, specificity, Jaccard scores (%) and absolute surface error (ASE) in mm^2 . Best results are in bold. Italic underlined scores highlight best results among learning schemes employed with U-Net.

convolutional filters. Models were implemented using Keras and trained on a recent desktop PC with a single Nvidia GeForce GTX 1080 Ti GPU with 11Gb/s. Once training is performed, predictions for one single axial slice take around 28ms only which is suitable for routine clinical practice.

We present Tab.I a comparative assessment of P, HP and A averaged over the whole pathological dataset. Reported results correspond to the best results among those obtained after each of the 10 training epochs. Italic underlined scores highlight best results achieved among the three configurations.

Dice results show higher performance when both healthy and pathological data are simultaneously used for training (A) with scores of 78.32% for deltoid, 81.58% for infraspinatus and 81.41% for subscapularis. Scheme A outperforms transfer learning and fine tuning (HP) from 4 to 7% in terms of Dice since HP only obtains 71.05% for deltoid, 77% for infraspinatus and 74.55% for subscapularis. However, this conclusion does not apply to supraspinatus for which A and HP schemes get the same performance in Dice ($\approx 65.7\%$). In particular, A increases the sensitivity (65.55% instead of 63.16%) but provides a slightly smaller specificity compared to HP. Comparing ASE from HP to A reveals improvements for all shoulder muscles including deltoid whose surface estimation error decreases from 268 to 105.5 mm^2 . The same finding arise when studying Jaccard scores whose gains are 7.8% and 6.5% for deltoid and subscapularis. Directly combining healthy and pathological data therefore appears as a better strategy than dividing training into two parts focusing on first healthy and then pathological data via transfer learning. Another finding brought by Tab.I is that exploiting annotations made on pathological shoulder muscles only (P) is the worst training strategy, especially for deltoid (Dice loss of 10% from A to P). It proves that CED features extracted from healthy examinations are suited enough for pathological anatomies while acting as an

efficient data augmentation strategy. Results for subscapularis deviate from this rule with higher similarity scores compared to HP combined with the best ASE (94.56 mm^2).

Accuracy scores for supraspinatus are globally worse than for other shoulder muscles since its thin and elongated shape can strongly vary across patients [16]. Moreover, we notice the presence of a single severely atrophied supraspinatus muscle (L-P-0922) among the set of pathological examinations. Dice results for this single muscle is 42.99% for P against 38.59% and 32.33% for HP and A. It suggests that muscles undergoing very strong degrees of injury must be processed separately, relying on pathological data only or manual delineations. Nevertheless, A appears globally better suited from weak to moderately severe muscle impairments.

Dedicated to the deltoid muscle, a comparison between P, HP and A is provided Fig.5 for each annotated slices of the whole pathological dataset. The top row displays Dice scores with respect to normalized axial slice number obtained by linearly scaling slice number from $[z_{min}, z_{max}]$ to $[0, 1]$ where $\{z_{min}, z_{max}\}$ are the minimal and maximal axial slice number displaying the deltoid. Overall, the bell-shape curves indicate that segmentation results are more accurate for mid-muscle regions than for both base and apex where muscles appear smaller with strong appearance similarities with surrounding tissues. Above conclusions ($A > HP > P$) are confirmed with much more individual Dice results grouped on the interval $[75, 95\%]$ for A. By studying the concordance between predicted and groundtruth deltoid surfaces (bottom row), we observe a stronger correlation for A than for P and HP with individual estimations closer to the line of perfect concordance (L-P-0773 is the most telling example).

Evaluation is supplemented by qualitative results given Fig.4 for deltoid (P, HP and A) and Fig.6 for rotator cuff muscles (A only). Displayed results cover the whole muscle spatial

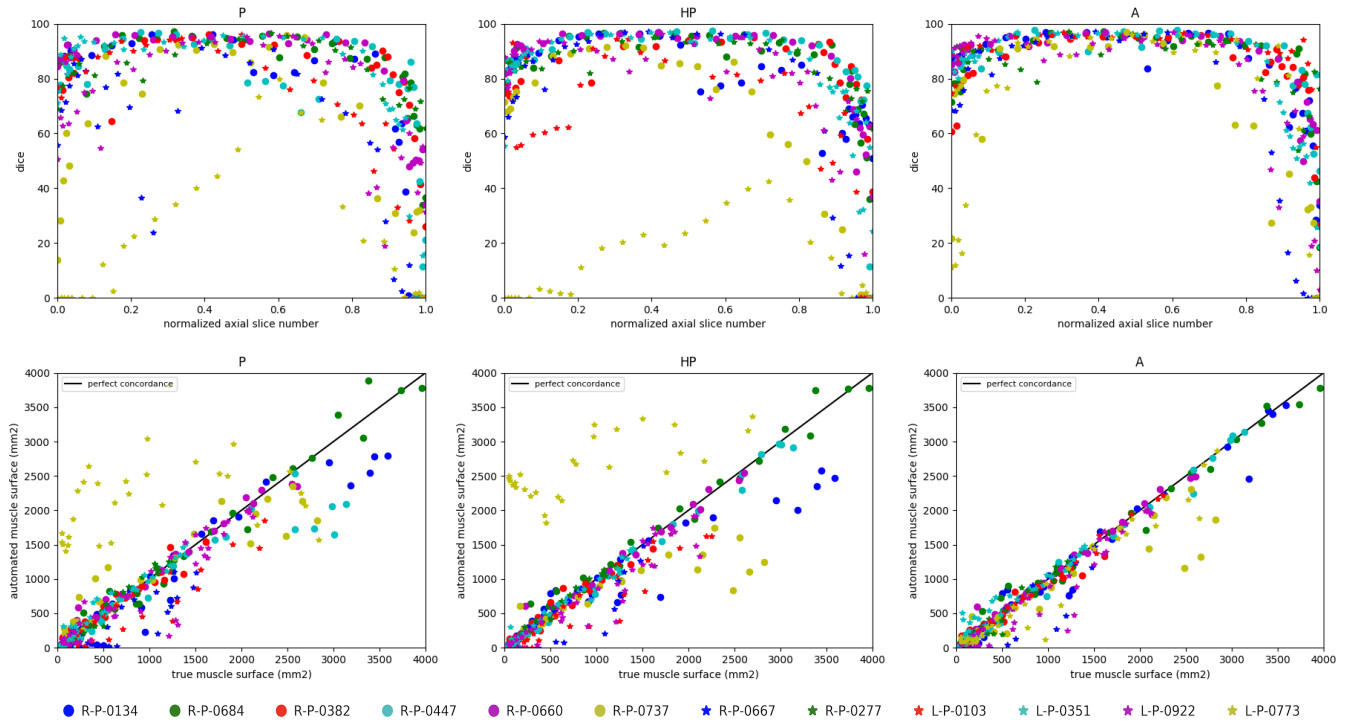


Fig. 5: Deltoid segmentation accuracy using U-Net [28] with learning schemes P, HP and A for each annotated slices of the whole pathological dataset. Top row show Dice scores with respect to normalized axial slice number. Bottom row displays concordance between groundtruth and predicted muscle surfaces in mm^2 . Black line indicates perfect concordance.

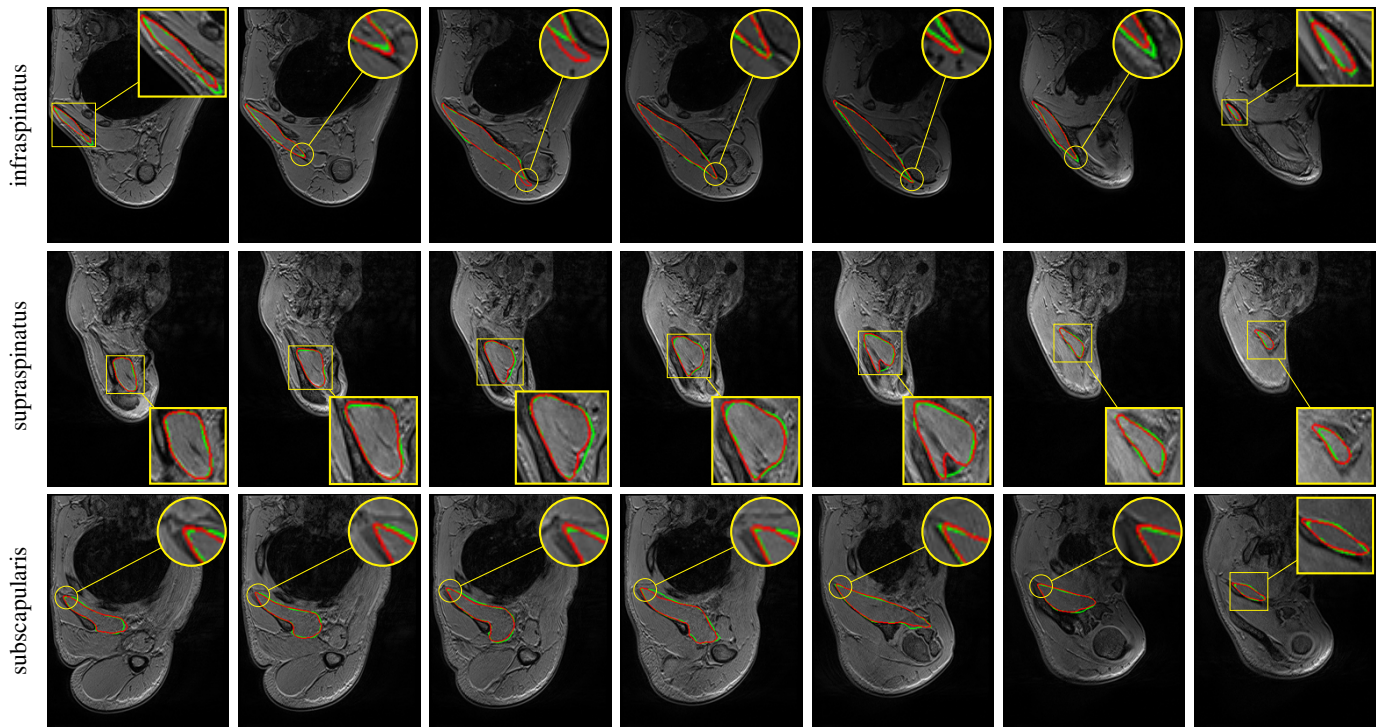


Fig. 6: Automatic pathological segmentation of infraspinatus, supraspinatus and subscapularis using U-Net [28] with training on both healthy and pathological data simultaneously (A). Groundtruth and estimated delineations are resp. in green and red. Displayed results cover whole muscle spatial extents resp. for R-P-0447, R-P-0660 and R-P-0134 examinations.

extents. We notice Fig.4 a very accurate deltoid delineation for A whereas P and HP tend to under-segment the muscle area. Complex muscle shapes and subtle contours illustrated Fig.6 are relatively well captured. In addition, we can notice outstanding performance near muscle insertion regions whose contours are usually hard to extract due to the vicinity with other structures. These results confirm that using simultaneously healthy and pathological data for training helps in providing good model generalizability despite the data scarcity issue combined with large appearance variabilities.

D. Extended deep convolutional architectures

The standard U-Net architecture [28] is extended Sect.III-C by exploiting VGG-16 as encoder, without (v16U-Net) or with (v16pU-Net) pre-trained weights based on ImageNet. Let us compare these three deep CEDs for pathological shoulder muscle segmentation through leave-one-out experiments. We rely on the best obtained training scheme (Sect.IV-C) combining healthy and pathological data (A). As previously, networks are trained with data augmentation, 10 epochs, a batch size of 10 images, Adam optimizer and a fuzzy Dice score as loss function. Learning rates change from U-Net and v16pU-Net (10^{-4}) to v16U-Net (5×10^{-5}) to avoid divergence for deep networks trained with random weights.

Tab.I indicate the performance reached by U-Net, v16U-Net and v16pU-Net over the whole pathological dataset with best scores in bold. It clearly shows that v16pU-Net globally outperforms U-Net and v16U-Net with Dice scores of 82.42% for deltoid, 81.98% for infraspinatus, 70.98% for supraspinatus and 82.80% for subscapularis. On the contrary, v16U-Net (resp. U-Net) obtains 80.05% (78.32%) for deltoid, 81.91% (81.58%) for infraspinatus, 67.30% (65.68%) for supraspinatus and 81.58% (81.41%) for subscapularis. In one hand, despite slightly worse scores compared with U-Net for infraspinatus in terms of sensitivity (83.74 against 84.61) and ASE (80.11 against 74.47mm²), v16U-Net is most likely to provide good predictive performance and model generalizability thanks to its deeper architecture. On the other hand, comparisons between v16U-Net and v16pU-Net reveals that pre-training the encoder using ImageNet brings non-negligible improvements. For instance, v16pU-Net provides significant gains for deltoid (resp. supraspinatus) whose Jaccard score goes from 71.46 (56.98) to 74% (61.31%). Surface estimation errors are among the lowest obtained with only 80.38mm² for deltoid and 82.95mm² for subscapularis. Despite their non-medical nature, the large amount of ImageNet images used for pre-training makes the network converge towards a better solution. v16pU-Net is therefore the most able to efficiently discriminate individual muscles from surrounding anatomical structures, compared to U-Net and v16U-Net. In average among the four shoulder muscles, gains for Dice, sensitivity and Jaccard reaches 2.8, 2.7 and 3.2% from U-Net to v16pU-Net.

Fig.7 focuses on the deltoid muscle to compare U-Net, v16U-Net and v16pU-Net for each annotated slices of the whole pathological dataset. As previously, comparisons are performed according to Dice scores (top row) and predicted versus groundtruth surface concordance (bottom row). From

U-Net to v16pU-Net, we can notice that individual Dice results are slightly pushed towards the upper limit (100%) with less variability and an increased overall consistency along axial slices, as for R-P-0737 and L-P-0773. Extreme axial slices are much better handled in the case v16pU-Net, especially when normalized slice numbers approach zero. In addition, compared to U-Net and v16U-Net, a slightly stronger correlation between predicted and groundtruth deltoid surface can be seen for v16pU-Net. Great improvements for R-P-0737 and L-P-0773 can be also highlighted.

Automatic pathological segmentation results given Fig.8 for deltoid, infraspinatus, supraspinatus and subscapularis using U-Net, v16U-Net and v16pU-Net allows to visually confirm the conclusions (v16pU-Net > v16U-Net > U-Net) given above. 8 pathological examinations among the 12 available are involved to give a complete overview. Globally, better contour adherence and shape consistency are reached by v16pU-Net whose ability to mimic expert annotations is notable. The great diversity in terms of textures (smooth in R-P-0684 versus granular in R-P-0737) is accurately captured despite high similar visual properties with surrounding structures. Visual results also reveal that v16pU-Net has a good behavior for complex muscle insertion regions (R-P-0447). Despite a satisfactory overall quality, U-Net and v16U-Net are frequently prone to under- (R-P-0134, R-P-0277) or over-segmentation (R-P-0684). Some examples report inconsistent shapes (R-P-0667, R-P-0737), sometimes combined with false positive areas located far away from the groundtruth muscle location (R-P-0447, L-P-0773). Using a pre-trained and complex architecture such as v16pU-Net to process simultaneously healthy and pathological data automatically provides accurate delineations of pathological shoulder muscles for patients with OPBB.

V. CONCLUSION

In this work, we successfully addressed automatic pathological shoulder muscle MRI segmentation for patients with obstetrical brachial plexus palsy by means of deep convolutional encoder-decoders. In particular, we studied healthy to pathological learning transferability by comparing different learning schemes in terms of model generalizability against large muscle shape, size, location, texture and injury variability. Moreover, convolutional encoder-decoder networks were expanded using VGG-16 encoders pre-trained on ImageNet to improve the accuracy reached by standard U-Net architectures. Our contributions were evaluated on four different shoulder muscles. First, results clearly show that features extracted from unimpaired limbs are suited enough for pathological anatomies while acting as an efficient data augmentation strategy. Compared to transfer learning, combining healthy and pathological data for training provides the best segmentation accuracy together with outstanding delineation performance for muscle boundaries including insertion areas. Second, experiments reveal that convolutional encoder-decoders involving a pre-trained VGG-16 encoder strongly outperforms U-Net. Despite the non-medical nature of pre-training data, such deeper networks are able to efficiently discriminate individual

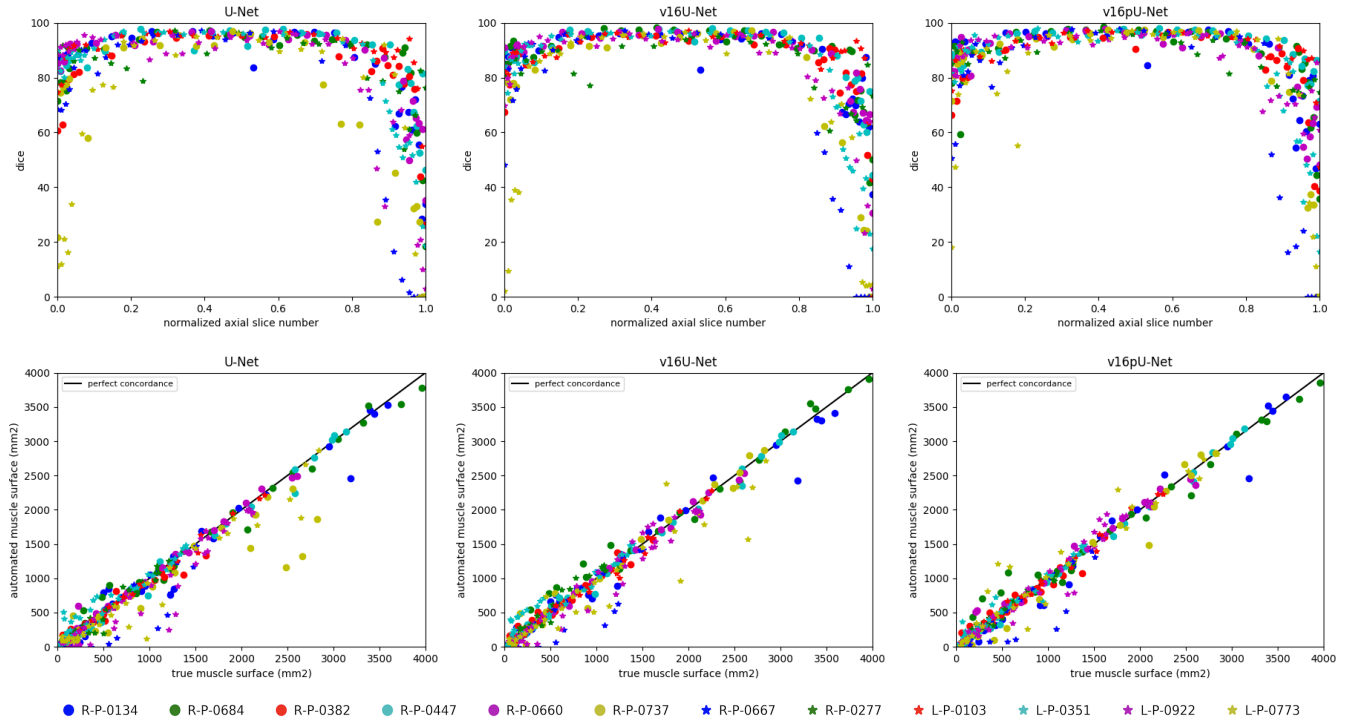


Fig. 7: Deltoid segmentation accuracy using U-Net [28], v16U-Net and v16pU-Net with learning scheme A for each annotated slices of the whole pathological dataset. Top row show Dice scores with respect to normalized axial slice number. Bottom row displays concordance between groundtruth and predicted muscle surfaces. Black line indicates perfect concordance.

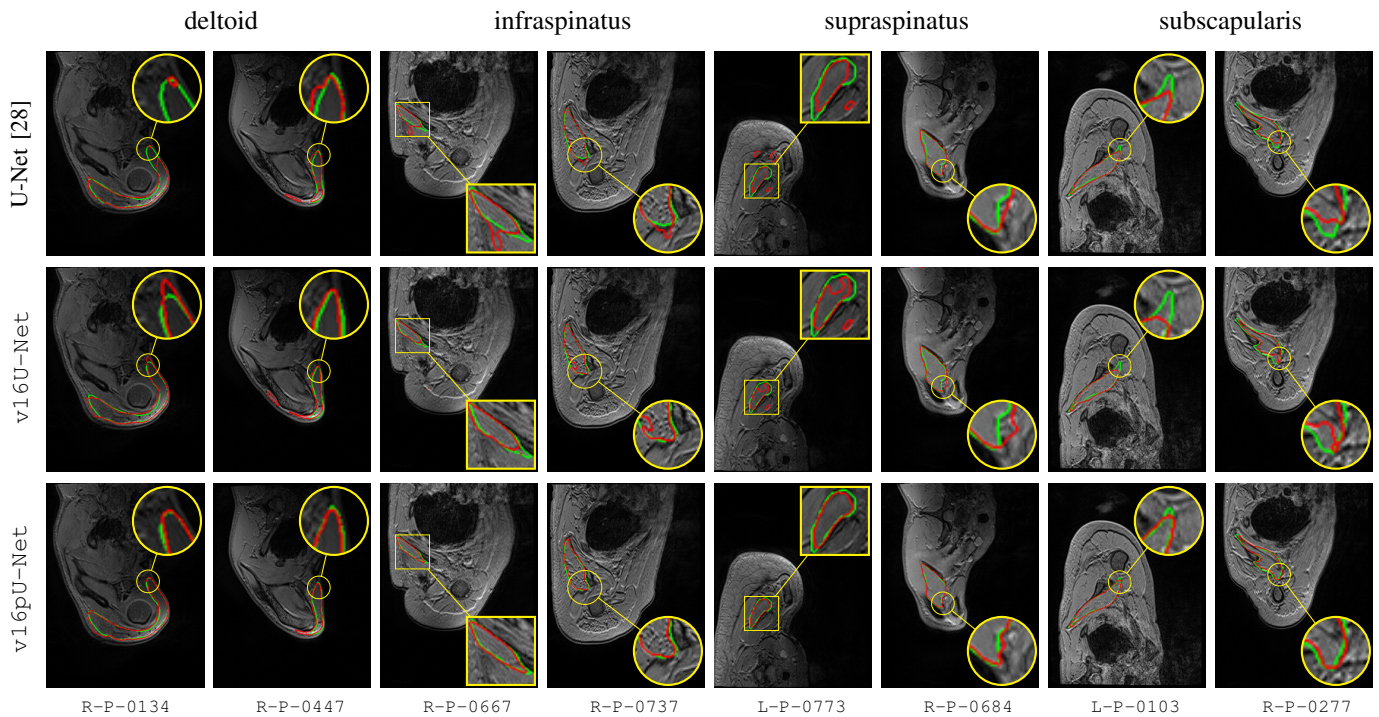


Fig. 8: Automatic pathological segmentation of deltoid, infraspinatus, supraspinatus and subscapularis using U-Net [28], v16U-Net and v16pU-Net with training on both healthy and pathological data simultaneously (A). Groundtruth and estimated delineations are resp. in green and red.

muscles from surrounding anatomical structures. The proposed approach can be easily extended to other muscle types and imaging modalities to provide clinical decision support in various applications including neuro-muscular diseases, sports related injuries or any other muscle disorders. These conclusions offer new perspectives for the management of musculo-skeletal diseases, even if a small and heterogeneous set of data is available. It paves the way for automatic inference of individual morphological parameters which are not accessible with simple clinical examinations. Our method could be useful to distinguish between pathologies, evaluate the effect of treatments and facilitate surveillance of neuromuscular disease progression. It could also be integrated into biomechanical models to improve the understanding of complex pathologies and help clinicians for intervention planning.

REFERENCES

- [1] C. Pons, F. T. Sheehan, H. S. Im, S. Brochard, and K. E. Alter, "Shoulder muscle atrophy and its relation to strength loss in obstetrical brachial plexus palsy," *Clinical Biomechanics*, vol. 48, pp. 80–87, 2017.
- [2] P. O'Berry, M. Brown, L. Phillips, and S. H. Evans, "Obstetrical brachial plexus palsy," *Current Problems in Pediatric and Adolescent Health Care*, vol. 47, no. 7, pp. 151–155, 2017.
- [3] S. P. Chauhan, S. B. Blackwell, and C. V. Ananth, "Neonatal brachial plexus palsy: incidence, prevalence, and temporal trends," in *Seminars in Perinatology*, vol. 38, no. 4, 2014, pp. 210–218.
- [4] S. Brochard, K. Alter, and D. Damiano, "Shoulder strength profiles in children with and without brachial plexus palsy," *Muscle & Nerve*, vol. 50, no. 1, pp. 60–66, 2014.
- [5] P. M. Waters, J. T. Monica, B. E. Earp, D. Zurakowski, and D. S. Bae, "Correlation of radiographic muscle cross-sectional area with glenohumeral deformity in children with brachial plexus birth palsy," *The Journal of Bone and Joint Surgery*, vol. 91, no. 10, p. 2367, 2009.
- [6] S. H. Kozin, "The evaluation and treatment of children with brachial plexus birth palsy," *The Journal of Hand Surgery*, vol. 36, no. 8, pp. 1360–1369, 2011.
- [7] A. Aydin, A. Biçer, T. Özkan, B. Mersa, S. Özkan, and Z. H. Yildirim, "Does primary brachial plexus surgery alter palliative tendon transfer surgery outcomes in children with obstetric paralysis?" *BMC Musculoskeletal Disorders*, vol. 12, no. 1, p. 74, 2011.
- [8] Y. Barnouin, G. Butler-Browne, T. Voit, D. Reversat, N. Azzabou, G. Leroux, A. Behin, J. S. McPhee, P. G. Carlier, and J.-Y. Hogrel, "Manual segmentation of individual muscles of the quadriceps femoris using MRI: a reappraisal," *Journal of Magnetic Resonance Imaging*, vol. 40, no. 1, pp. 239–247, 2014.
- [9] M. J. Tingart, M. Apreleva, J. T. Lehtinen, B. Capell, W. E. Palmer, and J. J. Warner, "Magnetic resonance imaging in quantitative analysis of rotator cuff muscle volume," *Clinical Orthopaedics and Related Research*, vol. 415, pp. 104–110, 2003.
- [10] G. Litjens, T. Kooi, B. E. Bejnordi, A. A. A. Setio, F. Ciompi, M. Ghahfoorian, J. A. van der Laak, B. Van Ginneken, and C. I. Sánchez, "A survey on deep learning in medical image analysis," *Medical Image Analysis*, vol. 42, pp. 60–88, 2017.
- [11] P.-H. Conze, C. Pons, V. Burdin, F. T. Sheehan, and S. Brochard, "Deep convolutional encoder-decoders for deltoid segmentation using healthy versus pathological learning transferability," in *IEEE International Symposium on Biomedical Imaging*, 2019.
- [12] C. Pons, B. Borotikar, M. Garetier, V. Burdin, D. B. Salem, M. Lempereur, and S. Brochard, "Quantifying skeletal muscle volume and shape in humans using mri: A systematic review of validity and reliability," *PLoS one*, vol. 13, no. 11, 2018.
- [13] A. Ogier, M. Sdika, A. Fouré, A. Le Troter, and D. Bendahan, "Individual muscle segmentation in MR images: A 3D propagation through 2D non-linear registration approaches," in *IEEE International Engineering in Medicine and Biology Conference*, 2017, pp. 317–320.
- [14] I. Südhoff, J. A. de Guise, A. Nordez, E. Jolivet, D. Bonnaeu, V. Khoury, and W. Skalli, "3D-patient-specific geometry of the muscles involved in knee motion from selected MRI images," *Medical & Biological Engineering & Computing*, vol. 47, no. 6, pp. 579–587, 2009.
- [15] E. Jolivet, E. Dion, P. Rouch, G. Dubois, R. Charrier, C. Payan, and W. Skalli, "Skeletal muscle segmentation from MRI dataset using a model-based approach," *Computer Methods in Biomechanics and Biomedical Engineering: Imaging & Visualization*, vol. 2, no. 3, pp. 138–145, 2014.
- [16] S. Kim, D. Lee, S. Park, K.-S. Oh, S. W. Chung, and Y. Kim, "Automatic segmentation of supraspinatus from MRI by internal shape fitting and autocorrection," *Computer Methods and Programs in Biomedicine*, vol. 140, pp. 165–174, 2017.
- [17] P.-Y. Baudin, N. Azzabou, P. G. Carlier, and N. Paragios, "Prior knowledge, random walks and human skeletal muscle segmentation," in *International Conference on Medical Image Computing and Computer-Assisted Intervention*, 2012, pp. 569–576.
- [18] S. Andrews and G. Hamarneh, "The generalized log-ratio transformation: learning shape and adjacency priors for simultaneous thigh muscle segmentation," *IEEE Transactions on Medical Imaging*, vol. 34, no. 9, pp. 1773–1787, 2015.
- [19] E. Ahmad, M. H. Yap, H. Degens, and J. S. McPhee, "Atlas-registration based image segmentation of MRI human thigh muscles in 3D space," in *Medical Imaging: Image Perception, Observer Performance, and Technology Assessment*, vol. 9037, 2014.
- [20] A. Le Troter, A. Fouré, M. Guye, S. Confort-Gouny, J.-P. Mattei, J. Gondin, E. Salort-Campana, and D. Bendahan, "Volume measurements of individual muscles in human quadriceps femoris using atlas-based segmentation approaches," *Magnetic Resonance Materials in Physics, Biology and Medicine*, vol. 29, no. 2, pp. 245–257, 2016.
- [21] C. M. Engstrom, J. Fripp, V. Jurcak, D. G. Walker, O. Salvado, and S. Crozier, "Segmentation of the quadratus lumborum muscle using statistical shape modeling," *Journal of Magnetic Resonance Imaging*, vol. 33, no. 6, pp. 1422–1429, 2011.
- [22] V. Barra and J.-Y. Boire, "Segmentation of fat and muscle from MR images of the thigh by a possibilistic clustering algorithm," *Computer Methods and Programs in Biomedicine*, vol. 68, no. 3, 2002.
- [23] S. Purushwalkam, B. Li, Q. Meng, and J. McPhee, "Automatic segmentation of adipose tissue from thigh magnetic resonance images," in *International Conference Image Analysis and Recognition*, 2013, pp. 451–458.
- [24] S. Orgiu, C. L. Lafortuna, F. Rastelli, M. Cadioli, A. Falini, and G. Rizzo, "Automatic muscle and fat segmentation in the thigh from T1-Weighted MRI," *Journal of Magnetic Resonance Imaging*, vol. 43, no. 3, pp. 601–610, 2016.
- [25] Y. LeCun, L. Bottou, Y. Bengio, and P. Haffner, "Gradient-based learning applied to document recognition," *Proceedings of the IEEE*, vol. 86, no. 11, pp. 2278–2324, 1998.
- [26] D. Cireşan, A. Giusti, L. M. Gambardella, and J. Schmidhuber, "Deep neural networks segment neuronal membranes in electron microscopy images," in *Advances in Neural Information Processing Systems*, 2012, pp. 2843–2851.
- [27] J. Long, E. Shelhamer, and T. Darrell, "Fully convolutional networks for semantic segmentation," in *IEEE Conference on Computer Vision and Pattern Recognition*, 2015, pp. 3431–3440.
- [28] O. Ronneberger, P. Fischer, and T. Brox, "U-Net: Convolutional networks for biomedical image segmentation," in *International Conference on Medical Image Computing and Computer-Assisted Intervention*, 2015, pp. 234–241.
- [29] Ö. Çiçek, A. Abdulkadir, S. S. Lienkamp, T. Brox, and O. Ronneberger, "3D U-Net: learning dense volumetric segmentation from sparse annotation," in *International Conference on Medical Image Computing and Computer-Assisted Intervention*, 2016, pp. 424–432.
- [30] F. Milletari, N. Navab, and S.-A. Ahmadi, "V-Net: Fully convolutional neural networks for volumetric medical image segmentation," in *International Conference on 3D Vision*, 2016, pp. 565–571.
- [31] K. Simonyan and A. Zisserman, "Very deep convolutional networks for large-scale image recognition," *arXiv preprint arXiv:1409.1556*, 2014.
- [32] O. Russakovsky, J. Deng, H. Su, J. Krause, S. Satheesh, S. Ma, Z. Huang, A. Karpathy, A. Khosla, M. Bernstein *et al.*, "ImageNet large scale visual recognition challenge," *International Journal of Computer Vision*, vol. 115, no. 3, pp. 211–252, 2015.
- [33] V. Iglovikov and A. Shvets, "TernausNet: U-Net with VGG11 encoder pre-trained on imagenet for image segmentation," *arXiv preprint arXiv:1801.05746*, 2018.
- [34] V. Iglovikov, S. Seferbekov, A. Buslaev, and A. Shvets, "TernausNetV2: Fully convolutional network for instance segmentation," *arXiv preprint arXiv:1806.00844*, 2018.
- [35] J. Yosinski, J. Clune, Y. Bengio, and H. Lipson, "How transferable are features in deep neural networks?" in *Advances in Neural Information Processing Systems*, 2014, pp. 3320–3328.